Strojniški vestnik - Journal of Mechanical Engineering 67(2021)4, 180-190
DOI:10.5545/sv-jme.2021.7124
Original Scientific Paper
Received for review: 2021-01-21
Received revised form: 2021-02-25
Accepted for publication: 2021-03-29
© 2021 Journal of Mechanical Engineering. All rights reserved.

Design of a Throat-extended FDM Extruder for Multi-axis 3D Printing

Hao Liu[1]* – Zhoupeng Liu[1,]* – Siting Hao[2]

[1] Nanjing University of Aeronautics and Astronautics, College of Mechanical and Electrical Engineering, China
[2] Tianjin University, College of Mechanical Engineering, China

Multi-axis fused deposition modelling (FDM) 3D printing technology has been paid attention to by more and more people. However, existing FDM extruders are usually short and fat, which significantly restricts the popularization of multi-axis FDM 3D printing technology because one significant trend of additive manufacturing is the use of long and thin extruders to avoid collisions between extruders and workpieces in the printing process. This paper presents the design of a throat-extended FDM extruder to print complex-shaped workpieces with details. The main contributions in this paper include: (i) presenting a novel extruder structure including an extended-throat, a smaller heater block, and a cooling mini-fan; (ii) designing an optimized heater block using the shapes of its components and the milling tool as constraints to make its volume as little small as possible; (iii) Construct experimental and simulation methods to examine the temperature distribution of the throat to optimize the shapes of the heat dams of nozzle throats and the wind speed of the heat-dissipation fan. Based on the throat-extended FDM extruder, a five-axis FDM 3D printer has been developed, and various complex-shaped workpieces have been printed without any support.
Keywords: 3D printing, FDM, extruder, design, multi-axis, throat

Highlights

- *Construct a novel FDM direct extruder structure, including a smaller heater block, the extended throat, and a mini cooling fan.*
- *Present experimental and simulation methods to measure the temperature distribution along the throat lengthwise direction referring to the heat-insulating tape and cooling-wind.*
- *Design an optimized heater block using shapes of its components and the milling tool as constraints to make its volume as small as possible.*
- *Optimize the heat dam number for the extended-throat shape using the orthogonal experiment method to prevent the heat conduction along the throat upward from the hot end as much as possible.*
- *Present an optimal wind speed for the mini cooling fan to make the thermal equilibrium state appear to maintain the working temperature of the heater block.*

0 INTRODUCTION

Along with increasing applications of 3D printing, researchers are increasingly dissatisfied with the 2.5-axis 3D printing because these supports waste significant amounts of printing time and materials **[1]**. Consequently, support-free multi-axis 3D printing has been popular in recent years **[2]** to **[4]**. Furthermore, in the field of surface-cladding, the multi-axis 3D printer has been regarded as the most appropriate type of equipment **[5]** and **[6]**. Among all 3D printing methods, fused deposition modelling (FDM) has been the most well-known method because of its simplicity and cheapness **[7]** and **[8]**. Therefore, this paper focuses on the FDM 3D printing that can be more easily extended to a multi-axis process from the 2.5-axis process by adapting the kinematics, extruders, and path planning **[1]** to **[3]**.

Among these adaptations, the improvement of extruders is very important because the conventional printing head is short and fat due to the hot end with a radiator and heater block, as shown in Fig. 1a. For many workpieces with complex structures **[9]** and **[10]**, when these details are going to be printed one by one so that printing paths are optimized, and the printing quality is improved, a conventional printing head is not suitable because the short-fat print head always collides printed workpiece details (see Fig. 1a). To avoid such collisions, an intuitive design concept is to extend the nozzle throat and to use a smaller hot end, as shown in Fig. 1b. Furthermore, the external radiator is eliminated.

There are two types of extruders: pellet extruders **[11]** to **[14]** and filament extruders **[15]** to **[18]**. For the first one, Pollák et al. **[11]** presented a pellet extruder that can use recycled materials as the printing material, except for plastic and composites. Whyman et al. **[12]** aimed at the special need that the bio-polymer filament could not satisfy for some research fields and designed a pellet-based extrusion system for the 3D printing of bio-polymers. Goyanes et al. **[13]** developed a single-step process pellet extruder that directly extrudes powder materials for the fabrication of drug products. Netto et al. **[14]** researched a twin-screw extruder to allow in-process multi-material mixing and direct deposition of the product to construct

*Corr. Author's Address: Nanjing University of Aeronautics and Astronautics, 054 Department, No.29 Yudao Street, Nanjing, China, liuhao-01@nuaa.edu.cn, liuzhoupenga@nuaa.edu.cn

three-dimensional parts. Regarding the background, a throat-extended pellet extruder may be appropriate. However, compared with filament extruders, pellet extruders are usually more expensive and complex. They are frequently used in special fields, such as biopolymers [12], drugs [13], composite materials [11] and [14], and where additive manufacturing can create furniture, vehicle bodies, or building materials [19] and [20]. Consequently, filament extruders are more suitable for most users of conceptual designs.

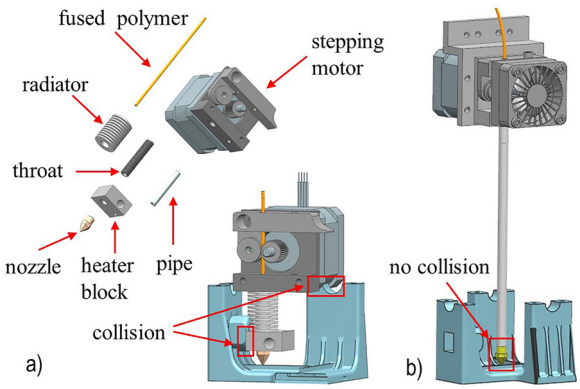

Fig. 1. *Comparison between the conventional printing head and the long-throat printing head; a) conventional printing head, and b) concept design of a multi-axis printing head*

The filament extruder includes a cool end and a hot end. The nozzle throat connects the two ends. The filament passes through the throat pipe. The cool end drives the filament into the hot end. It is usually composed of a numerical control motor, a toothed gear, and a bearing. The filament is placed between the toothed gear and the bearing. When the motor is activated, the gear rotates, and the filament is driven towards the hot end [15] and [16]. There are two types of filament extruders: direct extruders and Bowden extruders. The only difference between the two is that the throat of the direct extruder is a short and fat metal tube with a radiator while the throat of the Bowden extruder is a long flexible plastic tube [16] and [17]. Generally, there are two large disadvantages for the Bowden extruder [17]: (i) slower response time because of more friction in the Bowden tube to avoid stringing [21] to [23], fast retractions are required; (ii) a smaller range of materials, which means that some flexible filaments probably bind in Bowden tubes.

Consequently, researchers usually improve the direct extruder according to their needs. For example, Abilgaziyev et al. [16] presented a print head with several nozzles so that different materials can be printed in different regions of parts. Han et al. [18] developed a printing head with a nozzle and two throats so that two materials with different colours can be mixed. Go and Hart [24] found that the volumetric build rate of fused filament fabrication (FFF) could be limited by some conventional designs. They presented a Fast FFF system to overcome these conventional limits by extending the heater block towards the cool end and adding a laser auxiliary heater for the filament before coming into the heater block. Löffler and Koch [25] described a concept of a rotatable print head with a slot-shaped nozzle opening. Their design allowed the free adjustment of the path-line width and the layer heights. Though there are many works on innovative designs of direct extruders, there isn't an improved direct extruder to avoid collisions in multi-axis the 3D printing process even if Dai et al. [4] and Huang et al. [26] developed robot arms with direct extruders. To design a throat-extended slim direct extruder, there are three challenges: (i) shape optimization of a smaller heater block; (ii) shape optimization of nozzle throat without a radiator; (iii) appropriate temperature maintaining of the heater.

The heater is a key part of the extruder [15] and [27]. There are three problems to be improved: the resistor power, its appropriate temperature, and its geometrical shape. To select the power of the resistor, there are two estimation models of the heat flux: constant heat flux and constant wall temperature [27] to [29]. There are also some pieces of literature [30] to [32] to discuss appropriate temperatures to obtain the optimal printing quality. Because the appropriate temperature for a filament is constant and because aluminium (the heater block material) is a typical heat conductor, these conclusions in existing literature can be used in this paper. Jerez-Mesa's finite element analysis [33] also proved that the heater block has a constant temperature. However, distinct from existing designs, in our design, the heat-insulating tape method is used for our heater block because the ratio between the superficial area and the volume of the heater block is larger than the conventional heater block. The shape of the heater block in this paper is also optimized to reduce its *XY*-projection-area and quality.

Geometric accuracy is also an important topic about the FDM extruder. For example, Budzik et al. [37] verified the geometrical accuracy of 3D printing models of the lateral-mandibular condyle using several different printing methods, such as FDM, PolyJet, and selective laser sintering. The selective laser sintering had a standard deviation of 0.06 mm while FDM and PolyJet had a similar standard deviation of 0.07 mm. El-Katatny et al. [38] gave the standard deviation 0.24 % and 0.22 %, respectively, for FDM skull models and mandible models. Polak et al. [39] presented

FDM processing settings to the highest geometric accuracy. Boschetto and Bottini [40] developed an empirical formula to predict the geometric errors for FDM parts. In this paper, geometric accuracy comparisons between our extruder and the usual FDM extruder on the market are implemented to verify the *usability* of our extruder.

Aiming at the filament FDM extruder without collisions between the extruder and the workpiece in the printing process, the contributions of this paper include:

(1) Present a filament FDM extruder for the 3D printing of complex-structure workpieces. The extruder is composed of a heater block, an extended nozzle throat, and wind-speed-adjustable cooling equipment;
(2) Optimizing the shape of the heater block using other components and the milling tool as constraints to make its *XY*-projection-area as small as possible so that there are as few collisions as possible between the extruder and the workpiece in the printing process;
(3) Constructing FEA and experimental methods for the temperature distribution analysis of the throat to optimize the shapes of heat dams of nozzle throats and the wind speed of the heat-dissipation fan to prevent the heat conduction along the throat upward from the hot end.

In the rest of this paper, Section 1 provides the theoretical and experimental methods used to design the extruder. Section 2 presents details of the experimental set-up and the methods used to obtain the data. Section 3 shows the experimental data using figures and tables. Section 4 concludes our researches in this paper.

1 DESIGN AND METHODS

This section firstly gives a general design concept of the extruder. Then, a heater block shape optimization approach is presented based on the shapes and sizes of other components. The third subsection constructs a temperature field analysis FEA model for the heater block and the throat when the insulating tape and the cooling-fan are used. The fourth subsection discusses optimization methods for the heater block, the throat, and the cooling-wind speed.

1.1 General Design Concept

In this paper, the throat-extended extruder is installed in a five-axis (X, Y, Z, A, and C) printer. The printing head has three degree of freedom (DOF) including X, Y, and Z. The workpiece is placed on the AC rotary table, as shown in Fig. 2.

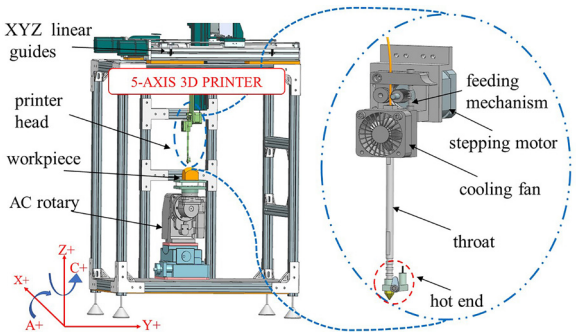

Fig. 2. *Concept design of our 5-axis FDM 3D printer with the throat-extended extruder*

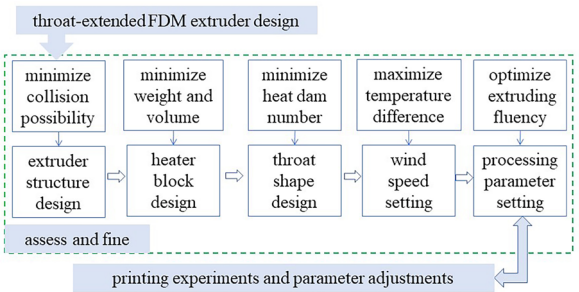

Fig. 3. *Design process proposed for the throat-extended FDM extruder*

To fabricate workpieces with fine details, the radiator has to be discarded, and the size of the heater block has to be reduced. Consequently, the design should include: (i) heater block shape optimization based on built-up members (nozzle, resistor, throat, thermistor), processing ability of machine tools; (ii) size and number optimization of dams of the nozzle throat based on the temperature field of the nozzle throat to the heat conduction along the throat upward from the hot end; (iii) wind speed adjustment to maintain the constant working temperature for the throat. Fig. 3 shows a flow diagram to design the FDM extruder.

1.2 Throat Design

A long and thin throat probably makes the filament form jam (see Fig. 4b) because of the extrusion force and the high throat temperature. The traditional extruder is equipped with radiators on the throat to radiate the throat heat, but they make the throat to thick. Consequently, throat heat dams and a cooling fan are used in the throat-extended extruder (see Fig. 4a).

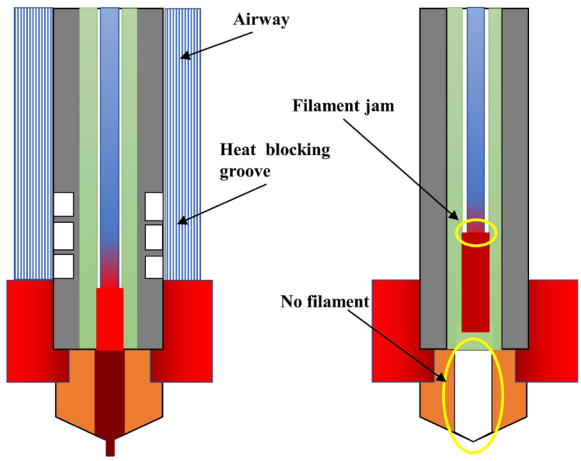

Fig. 4. *Schematic diagram of extruder jam; a) regularly work, b) jammed*

In our design, the throat is made of stainless steel. The wall thickness is 2 mm. There are several heat dams at the low region of the throat, shown in Fig. 4a. Widths for dams and grooves are 3 mm to 5 mm. The groove depth is 0.5 mm to 1.5 mm. The nozzle is made of copper. According to Fig. 2, the cooling wind blows from top to bottom. The velocity is 1 m/s to 5 m/s.

1.3 Heater Block Shape Design

As shown in Fig. 5a, the parts of a heater block include a nozzle, a resistor, a throat, and a thermistor. For the conventional heater block (see Fig. 5a), the main part is a quadrilateral aluminium block in which there are two large bolt holes for the nozzle and the throat, and a hole for the resistor that is inserted into the heater block. Because of the inserted resistor, the heater block is usually large. Existing aluminium blocks usually have the size 20 mm × 20 mm × 10 mm. Note that the resistor is horizontally inserted, which makes its electric wire occupy spaces in the length direction. The heater block occupies space up to 30 mm × 30 mm × 10 mm or more. Consequently, it is necessary to optimize the heater block shape. According to the 3D printing process, the design of the heater block of the throat-extended extrusion should satisfy the following principles:

(i) Aluminium block sizes in x-direction and y-direction should be as little as possible so that more workpieces details can be printed;

(ii) Temperature of the throat should be as low as possible so that the heat of heater block cannot be conducted to the cold end;

(iii) The quality of the heater block should be as little as possible because the large quality means that the large inertia force that makes the connection between the throat and the cold end loose.

Firstly, refer to the principle (iii). The quality of the heater block in the schematic in Fig. 5c, must be larger than the quality of the heater block in the scheme of Fig. 5b, which means that the schematic in Fig. 6c is against the criterion (iii). Consequently, we use the schematic in Fig. 5b instead of the one in Fig. 5c. Now we have to acquire some parameter values for the design in Fig. 5b to make the quality of the heater block as little as possible. These parameters are illuminated in Fig. 6. According to the ISO standard [34], because the depth of the screw thread groove of the throat is 0.541 mm, the wall thickness w (in Fig. 6) is usually larger than 1 mm. Because the diameter of the locking mini bolt is 3 mm, the thickness h (in Fig. 6) is usually larger than 3.6 mm [35].

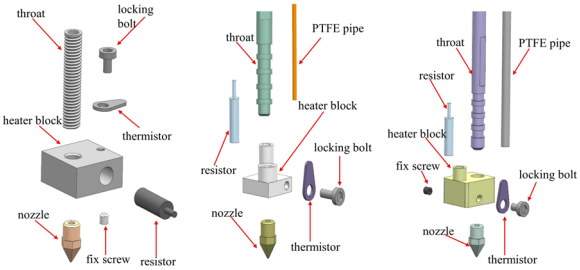

Fig. 5. *Comparison of a conventional heater block and our innovative heater block; a) conventional heater block, b) optimal heater block, c) inserted bolt hole*

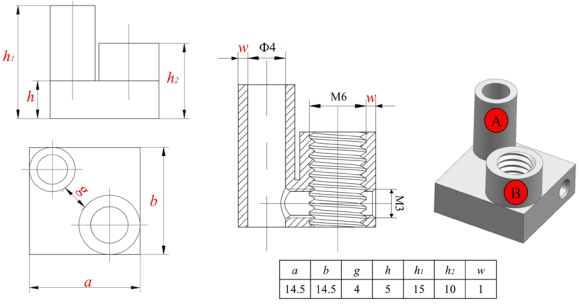

a	b	g	h	h1	h2	w
14.5	14.5	4	5	15	10	1

Fig. 6. *Size specification for the heater block [unit: mm]*

Criterion (ii) means that cylinder A and cylinder B (see Fig. 6) must be separated. By criterion (i), the less the gap size g is, the better the block is. However, the gap size g is determined by the diameter of the milling tool. Referring to existing milling tools, the minimum diameter of the milling tool is 3 mm. Consequently, we set the gap "g" as 4 mm so that the two cylinders can be milled and pasted with heat-insulating tape.

1.4 Principles and Methods of FEA

Since the cooling-wind is necessary to maintain a wanted thermal equilibrium state, the thermal numerical analysis problem is a heat transfer fluid-solid coupling problem that combines the computational fluid dynamics (CFD) computation of the environment flowing air and the temperature field FEA of the heater block. Principles of the fluid-solid coupling computation are shown in Fig. 7. The numerical analysis is implemented by Abaqus 6.14.

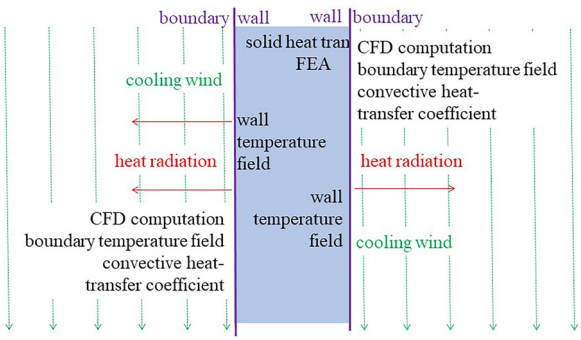

Fig. 7. *Illumination of the Fluid-Solid Interaction*

1.5 Orthogonal Experiment Statistical Methods

The orthogonal experiment is used to optimize the heat-dam shape and the cooling-wind speed. To analyse the orthogonal experiment data, two statistical methods (signal-to-noise ratio analysis (S/N) and analysis of variance (ANOVA)) are used. S/N is used to sort shape parameters of heat dams according to their importance. The statistical formula is used in Eq. (1), where η is S/N, p is the number of trials, and w is experimental data.

$$\eta = -10\log[\frac{1}{p}\sum_{i=1}^{p}(\frac{1}{w_i^2})]. \quad (1)$$

ANOVA is used to distinguish whether the difference in the experimental results is caused by the change of factor levels or by the experimental error, in which five statistical approaches are usually used: sum of squares (SS), mean square error (MS), degree of freedom (DOF), F-test statistics, and p-values. For the last one, the lower p-value (less than 0.05) means the significant influence of the parameter for the experimental result.

1.6 Temperature Field Analysis Model

As shown in Fig. 8, we select four temperature-monitoring points on the body composed of the throat and the heater block because we hope that the heater block has a constant temperature of 200 °C while the temperature declines as fast as possible along the throat. At the point near the cool end, the throat temperature should be close to the indoor temperature (20 °C).

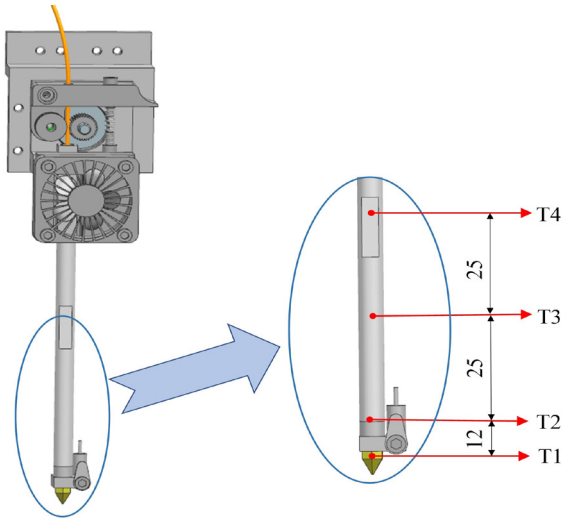

Fig. 8. *Thermal analysis model for the heater block and the throat; T1: heater block region, T2: throat region close to the hot end, T3: throat middle region, and T4: throat region close to the cool end*

2 EXPERIMENTAL DESCRIPTION

This section includes four subsections: extruder working environment and devices, thermal numerical analysis, discussions of experimental factors, and verification of FEA.

2.1 Working Environment and Devices

These experiments are performed at a room temperature of 20 °C. As shown in Fig. 9, the extruder is installed in the printer. We let the thermal resistor inserted in the heater block (see Fig. 5b) work while the extruder does not move but does extrude silks. There is a thermistor connected to a temperature controller. When the thermal equilibrium state appears, temperatures of these monitoring points are measured.

A temperature measurement system is shown in Fig. 10. The measurement range of the thermometer (Fig. 10, marked ①) is –200 °C to 1372 °C, and the accuracy is ±0.1 %. The speed range of the anemometer (see Fig. 10, marked ④) is 0 m/s to 30 m/s, with a basic error of ±1 %. The thermocouple

detector and the wire are fixed to install detectors at monitoring points.

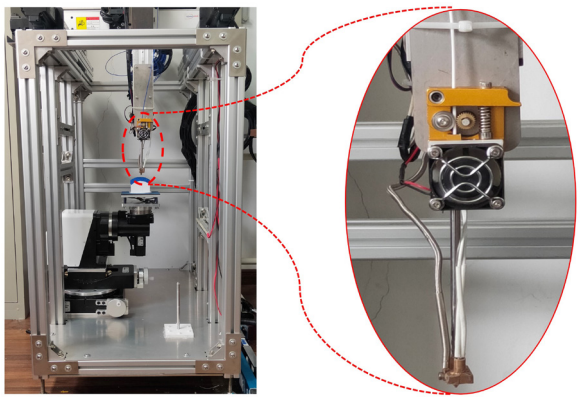

a) b)

Fig. 9. *Pictures of the 5-axis printer installed the novel extruder; a) overall appearance, and b) extruder*

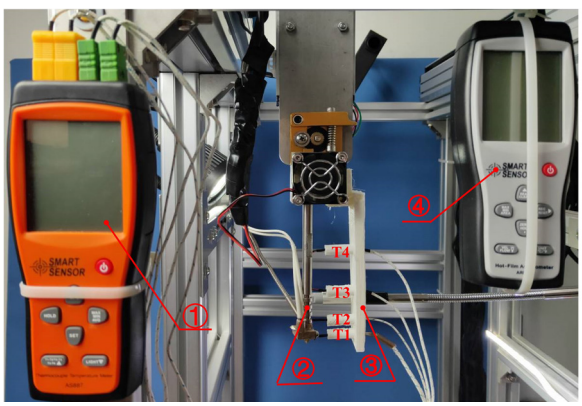

Fig. 10. *The experimental temperature measurement system; ① thermal conductor, ② extruder, ③ fixed support, and ④ mini-anemograph*

2.2 Thermal Numerical Analysis

The heater block is set as the heat source, and the boundary temperature is 200 °C, since only the thermal equilibrium is under consideration. The connection way between the components is "binding". The heat dissipation conditions are defined as the convective heat transfer between the surface of the throat and the outside air. Wind velocity conditions are assigned to the lower tuyere of the air guide hood. Since the wind velocity is not large, laminar flow is formed near the hot end. The convective heat transfer is obtained from the empirical formula in [36].

2.3 Experimental Factors and Levels

According to the analysis in subsection 2.1, a stainless-steel pipe is selected with a length of 140 mm, an outer diameter of 6 mm, an inner diameter of 4 mm as the throat pipe. The inside-liner is a Teflon tube with an outer diameter of 4 mm and an inner diameter of 1.9 mm. The filament is fed into the Teflon tube through the cold end and then arrives at the hot end. In the experiment, we select five factors that affect the temperature field distribution: wind velocity, the number of grooves, groove width, groove depth, and the dam width. Table 1 shows each level value of the factors, which is obtained based on experiences and preliminary experiments. We will select an optimal combination for these level values using an orthogonal experiment.

Table 1. *Factors and levels*

Levels	A Wind velocity [m/s]	B Groove number	C Dam width [mm]	D Groove width [mm]	E Dam depth [mm]
1	1	1	3	3	0.5
2	1.5	2	3.5	3.5	0.75
3	2	3	4	4	1.0
4	2.5	4	4.5	4.5	1.25
5	3	5	5	5	1.5

2.4 Verification of FEA

Because many samples are required for the optimizations of shapes and the parameters of the extruder, and real experiments always need more time and expense, we use simulation experiments instead of real experiments. To verify simulation results, this subsection measures the temperature of T_1 to T_4 in Fig. 8 under different heat dissipation conditions; the verification results are shown in Fig. 11. These results show that errors between FEA and real experiments are less than 2 %. Consequently, the FEA can replace the real experiment in this paper.

3 RESULT AND DISCUSSION

This section sorts factors in Table 1 according to their importance for the temperature field using the orthogonal experiment data analysed leveraging S/N and ANOVA methods.

3.1 Orthogonal Numerical Experimental Scheme

According to Table 1, we choose the orthogonal table of L_{25} (5^6) (see Table 2), which is composed of 25

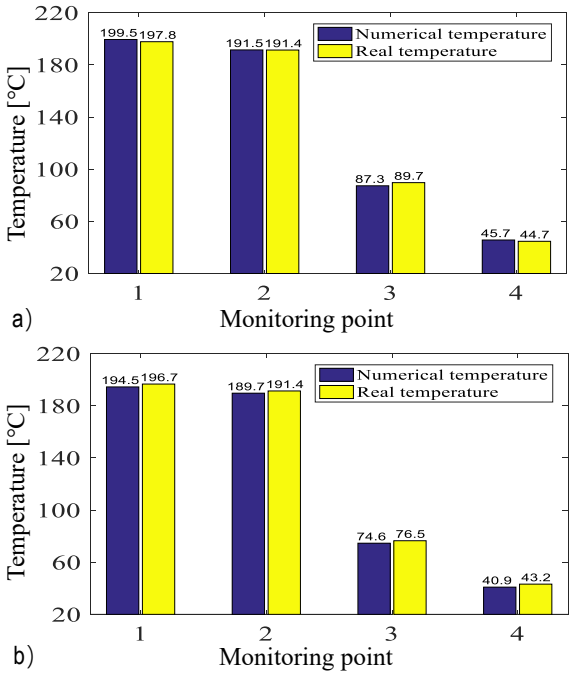

Fig. 11. *Comparison of simulation results and real results; a) wind speed is 3 m/s, and b) wind speed is 2 m/s*

Table 2. *Results and S/N of the orthogonal experiment*

No.	A	B	C	D	E	Result	S/N
1	1	1	1	1	1	133.61	42.517
2	1	2	3	4	5	149.26	43.479
3	1	3	5	2	4	149.76	43.508
4	1	4	2	5	3	144.07	43.171
5	1	5	4	3	2	142.52	43.078
6	2	1	5	4	3	144.50	43.197
7	2	2	2	2	2	142.72	43.090
8	2	3	4	5	1	140.97	42.983
9	2	4	1	3	5	148.27	43.421
10	2	5	3	1	4	156.39	43.884
11	3	1	4	2	5	152.52	43.667
12	3	2	1	5	4	150.66	43.560
13	3	3	3	3	3	150.14	43.530
14	3	4	5	1	2	149.43	43.489
15	3	5	2	4	1	146.38	43.310
16	4	1	3	5	2	146.73	43.330
17	4	2	5	3	1	149.68	43.503
18	4	3	2	1	5	159.68	44.065
19	4	4	4	4	4	158.48	43.999
20	4	5	1	2	3	153.71	43.734
21	5	1	2	3	4	152.07	43.641
22	5	2	4	1	3	153.42	43.718
23	5	3	1	4	2	152.5	43.665
24	5	4	3	2	1	150.51	43.551
25	5	5	5	5	5	162.98	44.243

(Note: The room temperature is 20 °C, and the thermal equilibrium temperature is 200 °C.)

experiments. The evaluation index is the temperature difference between T_2 and T_4 in Fig. 8, and the average value of each factor is calculated to obtain the range value.

3.2 Numerical Experimental Data Analysis

According to the range analysis in Table 3, the importance order of these factors can be concluded: A>E>B>C>D. Consequently, we can preliminarily infer that influences of wind velocity and dam depth are the largest.

Table 3. *Range analysis of the orthogonal experiment*

No.	A	B	C	D	E	blank
k1	143.84	145.89	147.75	150.51	144.23	149.59
k2	146.57	149.15	48.98	149.84	146.78	149.09
k3	149.83	150.61	150.61	148.54	149.17	148.91
k4	153.66	150.15	149.58	150.22	153.47	151.03
k5	154.30	152.40	151.27	149.08	154.54	149.57
R	10.45	6.51	3.52	1.97	10.31	---

To further highlight the influences of these factors, S/N analysis data are illuminated in Fig. 12, in which the level of these factors is taken as the abscissa. The strain S/N ratio is taken as a trend graph for every factor.

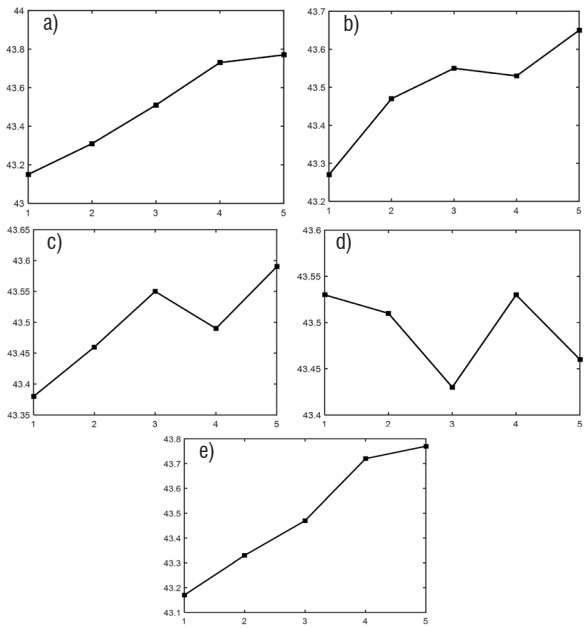

Fig. 12. *Main effect plot for S/N ratio; a) factor A, b) factor B, c) factor C, d) factor D, and e) factor E*

According to the S/N analysis diagram, we further analyse the influence of the level of each

factor. According to data in Table 3, we select the factor A, B, and E to conduct a second orthogonal test (see Table 4) because they have greater impact level values.

Table 4. *Preferred levels of designed parameters*

Factors	A	B	C	D	E
1	5(1)	5(1)	3	4.5	1.5(1)
2	5(1)	3(2)	3	4.5	1.25(2)
3	4(2)	5(1)	3	4.5	1.25(2)
4	4(2)	3(2)	3	4.5	1.5(1)

Analysis results of ANOVA are shown in Table 5, which shows the importance order is A>E>B>C>D. The experiment shows that wind velocity is the most important factor. Under the optimal wind velocity, shape parameters of heat dams are optimized to maximize the temperature difference. The result conforms to the main effect diagram.

Table 5. Analysis of variance (ANOVA)

Source	SS^2	*DOF*	*MS*	*F*	*p*
A	404.3	4	10.06	18.872	0.003
B	115.67	4	5.38	5.397	0.032
C	37.98	4	3.08	1.772	0.177
D	13.31	4	1.85	0.662	0.516
E	381.92	4	9.77	17.828	0.004
Error	13.9	4	1.86	---	---
Total	967.08	24	---	---	---

3.3 Orthogonal Real Experiments

According to the above analysis, we selected several parameters as the factors of a second orthogonal experiment (see Table 4): the wind velocity (A), the groove number (B), and the dam depth (E). Each of these factors takes two-level values. The level values of the factors C and D are fixed, and the L_4 (2^2) orthogonal test is designed. The experimental results consist of T_1, T_3, T_4, and *t*. The position of T is shown in Fig. 8, and *t* is the thermal equilibrium time.

Table 6. *The result of the real experiment*

No.	A	B	E	T_1	T_3	T_4	*t* [s]
1	1	1	1	189.2	90.2	36.1	148
2	1	2	2	188.5	86.9	33.3	151
3	2	1	2	180.4	72.7	35.1	121
4	2	2	1	178.9	71.3	37.1	118

As shown in Table 6, it is found that the temperature of the nozzle at 4 m/s is higher than that at 5 m/s, and the balance time is also lower than the latter, so the optimal wind velocity is 4 m/s. To make the temperature distribution more uniform, the optimal number of grooves is 5, the groove depth is 1.25 mm, and the optimal design parameter level is shown in Table 6.

3.4 Discussion on Experimental Results

According to the experimental data analysis, the following conclusions can be drawn:

(1) The temperature difference of the throat increases obviously along with the increase of wind speed. Therefore, this factor has the greatest influence on the temperature field. However, an excessive wind speed will increase the thermal equilibrium time and reduce the equilibrium temperature of the heater. The most suitable wind speed is 4 m/s.

(2) The groove plays an important role to prevent heat-conducting along the throat. It replaces the radiator and then reduces the volume of the hot end. The groove number is proportional to the temperature difference. The optimal groove number is 5.

(3) The groove depth is the third important factor. When there are 5 grooves, 1.25 mm to 1.5 mm groove depth is suitable. In consideration of the strength of the throat, 1.25 mm is optimal.

(4) The groove width and dam width are not significant. Therefore, 3 mm and 5 mm are selected, respectively, following the principle of maximum strength.

Table 7 lists optimal design parameters for the throat-extended extruder.

Table 7. *The optimum level of design parameters*

Factor	Wind velocity	Groove number	Dam width	Groove depth	Dam depth
Optimal level	4 m/s	5	3 mm	5 mm	1.25 mm

3.5 Manufacturing Accuracy Analysis

Six blocks with designed size 20 mm × 20 mm × 40 mm are printed by the extruder and a usual extruder using polylactic acid (PLA), acrylonitrile butadiene styrene (ABS), and polycarbonate (PC) materials, as shown in Fig. 13. The shape size, surface roughness and proper alignment are measured by the rough-meter, the micrometre calliper, and the dial indicator, respectively. These measured data are listed in Table 8, from which it can be found: (i) PLA has the highest geometrical accuracy, which is the reason that we use

PLA to test our 5-axis printer; (ii) blocks printed by our extruder and blocks printed by usual extruders have a similar geometrical accuracy, which shows that our extruder is valid.

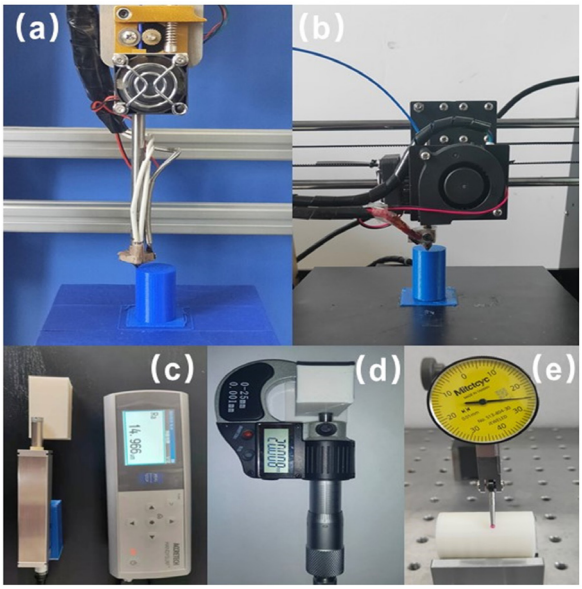

Fig. 13. *The printing process and measurement of the testing specimen; a) 5-axis printing, b) 3-axis printing, c) surface roughness measuring. d) dimension error measuring, e) proper alignment measuring*

Table 8. *Manufacturing accuracy of the testing specimen with different materials*

Properties	Type	PLA	ABS	PC
Surface roughness	3-axis	15.37	16.33	15.97
Ra [μm]	5-axis	13.54	15.89	15.67
Dimension error	3-axis	0.39	0.27	0.48
Δl [mm]	5-axis	0.15	0.33	0.25
Proper alignment	3-axis	Φ0.09	Φ0.15	Φ0.17
Δd [mm]	5-axis	Φ0.06	Φ0.12	Φ0.11

3.6 3D Printing Tests

To verify the effectiveness of the extruder, several workpieces are printed using the extruder. The experimental 5-axis printer and the extruder are shown in Fig. 10. The most suitable filament is PLA according to Table 8. Nozzles respectively with 0.4 mm, 0.6 mm, and 1.0 mm diameter are used in the extruder so that the printer can print several types of workpieces including 2.5-axis 3D printing with AC-axis periodical movement, five-axis linkage FDM cladding, and five-axis linkage 3D printing. The relationship among some 3D processing parameters and the fused filament volume $V_{printed}$ are:

$$V_{printed} = A \cdot s = [(w - h_f) \cdot h_f + \pi(\frac{h_f}{2})^2] \cdot s, \quad (2)$$

$$V_{printed} = S_f \cdot L. \quad (3)$$

In Eqs. (2) and (3), w is the fused material placement width, h_f is the layer height, s is the printing speed. The maximum of $V_{printed}$ in a unit time is closely related to the heater. It can be verified by experiments. The method to evaluate $V_{printed}$ is to extrude silk using the 1.0 mm nozzle while the speed s gradually increases until the nozzle is jammed. The maximum speed is 910 mm/min. Using the value, the maximum speed s for every nozzle can be calculated. S_f is the cross-section area of the filament. L is the extruded filament length. When $V_{printed}$, w, h_f, and S_f are given, s and L can be calculated. In this paper, we use the single factor experiment method to determine these optimal processing parameters. The optimal ones for different nozzles are listed in Table 9.

Table 9. *Process parameter values*

Diameter [mm]	h_f [mm]	w [mm]	s [mm/min]	L [mm]
0.4	0.2	0.2	2000	33.26
0.6	0.3	0.3	1500	56.13
1.0	0.5	0.5	700	72.56

(Note: h: layer height; w: silk placement width; s: print speed; L: extruded filament length)

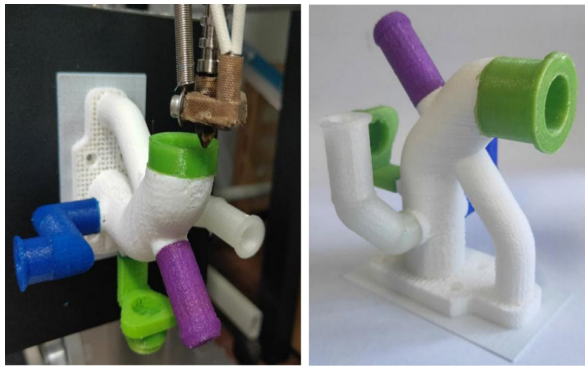

Fig. 14. *Multi-branch models printed by AC-axis periodical movement (nozzle diameter: 0.4 mm)*

Under the optimal level combination, nozzles with 0.4 mm, 0.6 mm, and 1.0 mm diameters are used in the extruder, and several workpieces are printed. From Fig. 14, we can find that distances between branch parts are restricted by sizes of the heater block in the x-direction and the y-direction because these parts cannot be printed at the same time. For Fig. 15a,

when a concave spherical surface is cladded, there is a similar colliding possibility for a conventional extruder. In Fig. 15b, several blades are printed.

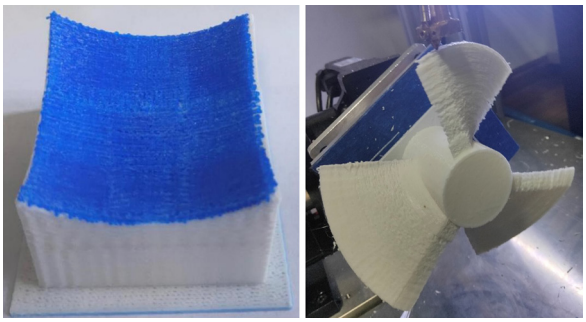

a) b)

Fig. 15. *Concave surface cladded and turbine printed by 5-axis linkage movement; a) 0.6 mm, and b) 1.0 mm*

4 CONCLUSIONS

This paper presents a throat-extended extruder so that a 5-axis FDM printer can print more details and clad more complex surfaces. Compared with a conventional filament FDM extruder, the throat-extended extruder is composed of a smaller heater block, an extended nozzle throat with heat dams, and wind-speed-adjustable cooling equipment. This paper optimizes those shapes and parameters by using several types of constraints: milling tools, heat-insulating tape, smaller *XY*-projection area of the heater block, a smaller quality of the heater block, the larger temperature difference between the hot end and cold end. The extruder is equipped with a 5-axis FDM printer. Several workpieces with complex shapes have been printed by the extruder using different types of nozzles. These experiments show the throat-extended extruder can steadily work in a 5-axis FDM printer with different nozzles. It can print various workpieces that cannot be printed with conventional FDM extruders.

5 ACKNOWLEDGEMENTS

This project is supported by the National Natural Science Foundation of China (Grant No. 51975281 and 51705183).

6 REFERENCES

[1] Wulle, F., Coupek, D., Schäffner, F., Verl, A., Oberhofer, F., Maier, T. (2017). Workpiece and machine design in additive manufacturing for multi-axis fused deposition modeling. *Procedia CIRP*, vol. 60, p. 229-234, **DOI:10.1016/j.procir.2017.01.046**.

[2] Liu, H., Liu, L., Li, D., Huang, R., Dai, N. (2020). An approach to partition workpiece cad model towards 5-axis support-free 3d printing. *The International Journal of Advanced Manufacturing Technology*, vol. 106, p. 683-699, **DOI:10.1007/s00170-019-04495-3**.

[3] Wei, X., Qiu, S., Zhu, L., Feng, R., Tian, Y., Xi, J., Zheng, Y. (2018). Toward Support-Free 3D Printing: A Skeletal Approach for Partitioning Models. *IEEE Transactions on Visualization and Computer Graphics*, vol. 24, no. 10, p. 2799-2812, **DOI:10.1109/TVCG.2017.2767047**.

[4] Dai, C., Wang, C.C. L., Wu, C., Lefebvre, S., Fang, G., Liu, Y.-J. (2018). Support-free volume printing by multi-axis motion. *ACM Transactions on Graphics*, vol. 37, no. 4, p. 1-14, **DOI:10.1145/3197517.3201342**.

[5] Calleja, A., Tabernero, I., Fernández, A., Celaya, A., Lamikiz, A., López de Lacalle, L.N. (2014). Improvement of strategies and parameters for multi-axis laser cladding operations. *Optics and Lasers in Engineering*, vol. 56, p. 113-120, **DOI:10.1016/j.optlaseng.2013.12.017**.

[6] Kapil, S., Negi, S., Joshi, P., Sonwane, J., Sharma, A., Karunakaran, K.P. (2017). 5-axis slicing methods for additive manufacturing process. *Proceedings of the 28th Annual International Solid Freeform Fabrication Symposium*, p. 1886-1896.

[7] Saeed Daneshmand, S., Aghanajafi, C. (2012). Description and modeling of the additive manufacturing technology for aerodynamic coefficients measurement. *Strojniški vestnik-Journal of Mechanical Engineering*, vol. 58, no. 2, p. 125-133, **DOI: 10.5545/sv-jme.2010.238**.

[8] Budzik, G., Burek, J., Bazan, A., Turek, P. (2016). Analysis of the accuracy of reconstructed two teeth models manufactured using the 3DP and FDM technologies. *Strojniški vestnik - Journal of Mechanical Engineering*, vol. 62, no. 1, p. 11-20, **DOI:10.5545/sv-jme.2015.2699**.

[9] Valentan, B., Brajlih, T., Drstvenšek, I., Balič, J. (2011). Development of a part-complexity evaluation model for application in additive fabrication technologies. *Strojniški vestnik - Journal of Mechanical Engineering*, vol. 57, no. 10, p. 709-718, **DOI:10.5545/sv-jme.2010.057**.

[10] Homar, D., Pušavec, F. (2017). The development of a recognition geometry algorithm for hybrid – subtractive and additive manufacturing. *Strojniški vestnik - Journal of Mechanical Engineering*, vol. 63, no. 3, p. 151-160, **DOI:10.5545/sv-jme.2016.3924**.

[11] Pollák, M., Kaščak, J., and Tkáč, J. (2019). Design of the 3D printhead with extruder for the implementation of 3D printing from plastic and recycling by industrial robot. *TEM Journal*, vol. 8, no. 3, p. 709-713, **DOI:10.18421/TEM83-02**.

[12] Whyman, S., Arif, K.M., Potgieter, J. (2018). Design and development of an extrusion system for 3D printing biopolymer pellets. *The International Journal of Advanced Manufacturing Technology*, vol. 96, p. 3417-3428, **DOI:10.1007/s00170-018-1843-y**.

[13] Goyanes, A., Allahham, N., Trenfield, S.J., Stoyanov, E., Gaisford, S., Basit, A.W. (2019). Direct powder extrusion 3D printing: Fabrication of drug products using a novel single-step

process. *International Journal of Pharmaceutics*, vol. 567, **DOI:10.1016/j.ijpharm.2019.118471**.

[14] Justino Netto, J.M., Silveira, Z.D.C. (2018). Design of an innovative three-dimensional print head based on twin-screw extrusion. *ASME Journal of Mechanical Design*, vol. 140, no. 12, art. ID 125002, **DOI:10.1115/1.4041175**.

[15] Gibson, I., Rosen, D., Stucker, B. (2015). *Additive Manufacturing Technologies,* Springer, New York.

[16] Abilgaziyev, A., Kulzhan, T., Raissov, N., Ali, M.H., Match, W.L.KO., Mir-Nasiri, N. (2015). Design and development of multi-nozzle extrusion system for 3D printer. *International Conference on Informatics, Electronics & Vision*, **DOI:10.1109/ICIEV.2015.7333982**.

[17] Obias Hullette, All3DP, Direct vs Bowden Extruder: Does It Make a Difference? from *https://all3dp.com/2/direct-vs-bowden-extruder-technology-shootout/*, accessed on 2020-10-01.

[18] Han, S., Xiao, Y., Qi, T., Li, Z., Zeng, Q. (2017). Design and analysis of fused deposition modeling 3D printer nozzle for color mixing. *Advances in Materials Science and Engineering*, art. ID 2095137, **DOI:10.1155/2017/2095137**.

[19] Fok, K.-Y., Cheng, C.-T., Ganganath, N., Iu, H.H.-C., Tse, C.K. (2019). An ACO-based tool-path optimizer for 3-D printing applications. *IEEE Transactions on Industrial Informatics*, vol. 15, no. 4, p. 2277–2287, **DOI:10.1109/TII.2018.2889740**.

[20] Abdulhameed, O., Al-Ahmari, A., Ameen, W., Mian, S.H. (2019). Additive manufacturing: challenges, trends, and applications. *Advances in Mechanical Engineering*, vol. 11, no. 2, **DOI:10.1177/1687814018822880**.

[21] Jin, Y., He, Y., Fu, J., Gan, W., Lin, Z. (2014). Optimization of tool-path generation for material extrusion-based additive manufacturing technology. *Additive Manufacturing*, vol. 1-4, p. 32-47, **DOI:10.1016/j.addma.2014.08.004**.

[22] Duty, C.E., Love, L.J. (2015). Big Area Additive Manufacturing (BAAM), Cincinnati Incorporated, from *https://www.e-ci.com/baam/*, accessed on 2021-04-10, **DOI:10.2172/1210140**.

[23] Molitch-Hou, M. (2018). Overview of Additive Manufacturing Process. Zhang, J., Jung, Y-G. (eds.) *Additive Manufacturing*, Elsevier, p. 1-38, **DOI:10.1016/B978-0-12-812155-9.00001-3**.

[24] Go, J., Hart, A.J. (2017). Fast desktop-scale extrusion additive manufacturing. *Additive Manufacturing*, vol. 18, p. 276-284, **DOI:10.1016/j.addma.2017.10.016**.

[25] Löffler, R., Koch, M. (2019). Innovative extruder concept for fast and efficient additive manufacturing. *IFAC-PapersOnLine*, vol. 52, no. 10, p. 242-247, **DOI:10.1016/j.ifacol.2019.10.071**.

[26] Huang, B., Singamneni, S.B. (2015). Curved layer adaptive slicing (CLAS) for fused deposition modelling. *Rapid Prototyping Journal*, vol. 21, no. 4, p. 354-367, **DOI:10.1108/RPJ-06-2013-0059**.

[27] Turner, B.N., Strong, R., nd A. Gold, S.A. (2014). A review of melt extrusion additive manufacturing processes: I. Process Design and Modeling. *Rapid Prototyping Journal*, vol. 20, no. 3, p. 192-204, **DOI:10.1108/RPJ-01-2013-0012**.

[28] Bellini, A., Güçeri, S., Bertoldi, M. (2004). Liquefier dynamics in fused deposition. *Journal of Manufacturing Science and Engineering*, vol. 126, no. 2, p. 237-246, **DOI:10.1115/1.1688377**.

[29] Ramanath, H.S., Chua, C.K., Leong, K.F., Shah, K.D. (2008). Melt flow behavior of poly-ε-caprolactone in fused deposition modelling. *Journal of Materials Science: Materials in Medicine*, vol. 19, no. 7, p. 2541-2550, **DOI:10.1007/s10856-007-3203-6**.

[30] Manikandan, N., Vignesh, T., Prasath, C., Ismail, M. (2020). Thermo-mechanical analysis of fused filament fabrication process. *IOP Conference Series: Materials Science and Engineering*, vol. 764, p. 012008, **DOI:10.1088/1757-899X/764/1/012008**.

[31] Lužanin, O., Movrin, D., Plančak, M. (2013). Experimental investigation of extrusion speed and temperature effects on arithmetic mean surface roughness in FDM built specimens. *Journal for Technology of Plasticity*, vol. 38, no. 2, p. 179-189, **DOI:10.1007/s00170-019-03859**.

[32] Kozior, T., Mamun, A., Trabelsi, M. (2020). Quality of the surface texture and mechanical properties of FDM printed samples after thermal and chemical treatment. *Strojniški vestnik - Journal of Mechanical Engineering*, vol. 66, no. 2, p. 105-113, **DOI:10.5545/sv-jme.2019.6322**.

[33] Jerez-Mesa, R., Travieso R. (2015). Design of open source 3D printer extruder and modelling of thermal performance with FEA. *19th International Research/Expert Conference: Trends in the Development of Machinery and Associated Technology*.

[34] ISO 724:1993(E). *ISO General-Purpose Metric Screw Threads - Basic Dimensions*. International Organization for Standardization, Geneve.

[35] ANSI H35.2(M) (2017). *American National Standard Dimensional Tolerances for Aluminum Mill Products*. American National Standards Institute. America.

[36] Mert P., Hakan D. (2020). An experimental study for determination of convective heat transfer coefficients on cooling monofilament. *International Journal of Heat and Mass Transfer*, vol. 149, no. 3, p. 11925-11936, **DOI:10.1016/j.ijheatmasstransfer.2019.119255**.

[37] Budzik, G., Turek, P., Dziubek, T., Gdula, M. (2020). Elaboration of the measuring procedure facilitating precision assessment of the geometry of mandible anatomical model manufactured using additive methods. *Measurement and Control*, vol. 53, no. 1-2, p. 181-191, **DOI:10.1177/0020294019881708**.

[38] El-Katatny I., Masood, S.H., Morsi, Y.S. (2010). Error analysis of FDM fabricated medical replicas. *Rapid Prototyping Journal*, vol. 16, no. 1, p. 36-43, **DOI:10.1108/13552541011011695**.

[39] Polak, R., Sedlacek, F., Raz, K. (2017). Determination of FDM printer settings with regard to geometrical accuracy. *Proceedings of the 28th DAAAM International Symposium*, p. 0561-0566, **DOI:10.2507/28th.daaam.proceedings.079**.

[40] Boschetto, A., Bottini, L. (2014). Accuracy prediction in fused deposition modeling. *The International Journal of Advanced Manufacturing Technology*, vol. 73, p. 913-928, **DOI:10.1007/s00170-014-5886-4**.